https://doi.org/10.5194/egusphere-2025-4434
Preprint. Discussion started: 4 October 2025

Long-term measurements of wind and turbulence from a calibrated 1290 MHz radar wind profiler at the Eastern North Atlantic atmospheric observatory

August Mikkelsen[1], Virendra P. Ghate[2], Daniel T. McCoy[1], Hamish Gordon[3]

[1]Department of Atmospheric Science, University of Wyoming, Laramie, WY, USA
[2] Environmental Science Division, Argonne National Laboratory, Lemont, IL, USA
[3]Department of Chemical Engineering and Center for Atmospheric Particle Studies, Carnegie Mellon University, Pittsburgh, PA, USA

Correspondence to: August Mikkelsen (amikkels@uwyo.edu)

https://doi.org/10.5194/egusphere-2025-4434
Preprint. Discussion started: 4 October 2025

ABSTRACT

Turbulence in the marine boundary layer is closely coupled with the physical properties of marine boundary layer clouds. However, these turbulent motions are difficult to observe, resulting in very few observations of turbulence properties over the open oceans. In this work data collected by the 1290 MHz Radar Wind Profiler (RWP) part of the Atmospheric Radiation Measurement (ARM) Eastern North Atlantic (ENA) site are used to characterize winds and boundary layer turbulence. The RWP wind, precipitation long pulse and precipitation short pulse modes were calibrated using the surface laser disdrometer. Over the 10 years of data analyzed here, the RWP wind mode calibration constant, sensitivity, and dynamic range fluctuated between -84 to -44 dB, -15 to 9 dBZ, and 12 to 21 dBZ, respectively. The clear-air RWP echoes were used to derive structure function of the refractive index (Cn^2) and dissipation rates of turbulence kinetic energy (ε). Both Cn^2 and ε decreased from surface upwards with higher values in the winter months and lower values in the summer months consistent with previous studies. Despite the marine location, the ε was affected by island heating during southerly wind conditions. The results reported herein have implications for RWP operational research and climatological studies at the ARM ENA site.

https://doi.org/10.5194/egusphere-2025-4434
Preprint. Discussion started: 4 October 2025

1 Introduction

Marine low clouds cover vast areas of the Eastern subtropical oceans and persist almost year-round. Marine boundary layer clouds are intimately coupled to the turbulence in the boundary layer that is modulated by surface fluxes, cloud top radiative cooling, wind shear, precipitation and entrainment (Wood, 2012). These clouds have a net cooling effect on the Earth as they reflect much greater amount of solar radiation back to space as compared to the underlying ocean surface, while still emitting longwave radiation similar to that of the ocean surface due to their low cloud top heights (Hartmann and Short, 1980). Hence, these clouds are an important component of the Earth's radiation budget and need to be accurately represented in a range of atmospheric models. Despite their importance, even the most advanced ESMs struggle to accurately simulate these clouds, partly due to inadequate understanding and representation of the multi-scale processes modulating the clouds and the boundary layer turbulence.

Radar wind profilers (RWPs) have been long used to observe and study winds, turbulence, and depth of the boundary layer. The National Oceanic and Atmospheric Administration (NOAA) profiler network (NPN) reports boundary layer winds that are used for weather forecasting (https://psl.noaa.gov/data/obs/datadisplay/). Similar efforts are made in Europe under the European National Meteorological Services (EUMETNET) Profiling Program (E-PROFILE) that also includes RWPs (Illingworth et al. 2019). The data from these profilers have been used to estimate structure function parameters of refractive index and turbulence (Gossard et al., 1998; McCaffrey et al., 2017; White et al., 1999) etc.) and estimate depth of the planetary boundary layer (e.g. Bianco et al., 2008; Molod et al., 2015 etc.). More recently, RWP data has also been utilized to characterize vertical air motions within deep convective clouds (Wang et al., 2020) and the associated precipitation drop size distributions (Williams, 2016).

The Atmospheric Radiation Measurement (ARM) user facility operates instruments at multiple sites to collect atmospheric observations. One such site is located on the island of Graciosa in the Açores, called the Eastern North Atlantic (ENA) observatory (Mather and Voyles, 2013) (Figure 1). The ENA site hosts multiple instruments for characterizing aerosol, cloud, radiation, dynamic and thermodynamic fields including an RWP (Wang et al., 2022; Wood et al., 2015). Although the site was constructed primarily to study marine boundary layer clouds, it encounters range of cloud and weather phenomenon

https://doi.org/10.5194/egusphere-2025-4434
Preprint. Discussion started: 4 October 2025

(Rémillard and Tselioudis, 2015). The data from this site has been used to study processes related to boundary layer turbulence, aerosol, cloud, and aerosol-cloud-radiation interactions (Ghate et al., 2021, 2023; Qiu et al., 2024; Wang et al., 2021 and others).

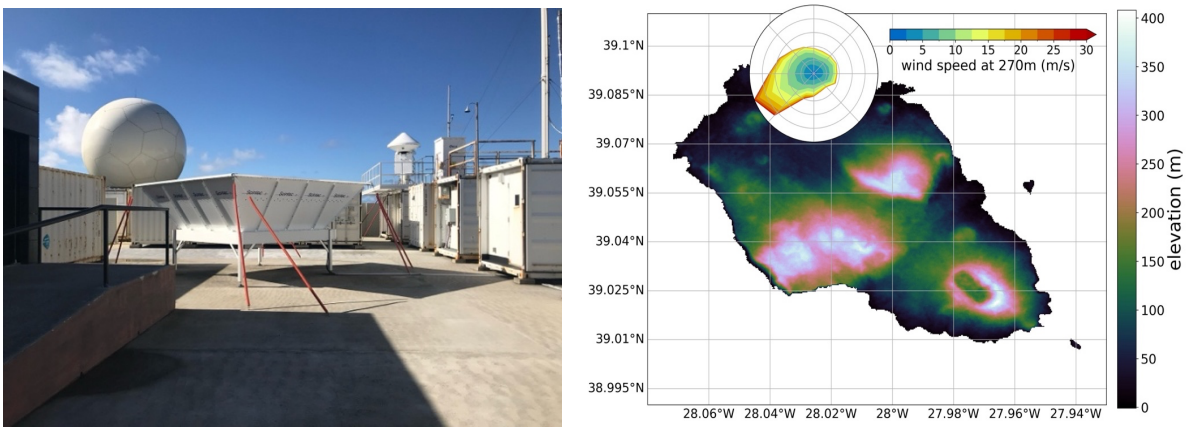

Figure 1 (a) Image of 1290 MHz radar wind profiler at ENA. (b) Topography of Graciosa Island overlaid by mean winds observed by the RWP profiler at 270m (windrose). The windrose is centered on the location of ENA.

In this study we showcase the efficacy of the RWP at the ARM ENA site for studying marine boundary layer clouds and qualify when it is valid for scientific study. Section 2 describes the data and the instrumentation used for this work. In Section 3, we focus on the noise-filtering, sensitivity and calibration of the RWP. In Section 4 we derive the structure function parameter of refractive index (C_n^2) and TKE dissipation rate (ε) from RWP measurements. In Section 5, we examine the climatology of wind and turbulence conditions at ENA through the RWP, providing a baseline of valid wind retrievals made during the nearly 10 years of this instrument's operation (at time of writing). And finally, our findings are summarized in Section 6. The goal of this work is to illustrate the feasibility of the RWP at the ENA site for deriving these parameters, establish guidance for when the instrument should not be used at this site, and to examine the climatology of winds on Graciosa Island.

https://doi.org/10.5194/egusphere-2025-4434
Preprint. Discussion started: 4 October 2025

2 Data and Instrumentation

In this section, all input datastreams used in this study are briefly described. The ARM ENA site has been operational since 2013, hosting multiple instruments. Described below are instruments data from which were used in this work.

2.1 1290 MHz Radar Wind Profiler

1290 MHz RWP has been operational the ENA site from September 10th, 2014, to the time of writing (February 2025). In that time, it has been operating nigh-continuously except for a period between July 8, 2019, and September 14th, 2020 (Muradyan and Ermold, 2021d, c, b). This 14 month downtime comes as a result of heavy corrosion to the antenna and phase shifter, which could not be repaired; new components were purchased and installed, and the instrument returned to service (Muradyan and Coulter, 2020).

The RWP operates in 3 modes: wind mode, short-pulse precipitation mode and long-pulse precipitation mode. The wind mode has three beams, cycling sequentially between vertically pointing mode and two oblique modes. All the modes collect raw Doppler spectra and its first three moments. By utilizing consensus in radial velocity, the measurements from the wind modes are used to derive 10-minute averaged consensus winds profiles. Between each wind mode measurement, 2 vertically pointing precipitation modes are operated: a long-range high-sensitivity precipitation mode with a longer pulse length and a short-range low-sensitivity precipitation mode with a shorter pulse length. A full cycle of all 5 beams takes roughly 53 seconds. Pertinent operating details for the RWP's 5 beam configuration modes can be found in Table 1.

Table 1: Operational Characteristics of RWP and KAZR

	RWP			**KAZR**
Mode	Wind	Precipitation Long Pulse (High)	Precipitation Short Pulse (Low)	General
Frequency (GHz)	1.290			34.83
Wavelength (mm)	232.55			8.61

https://doi.org/10.5194/egusphere-2025-4434
Preprint. Discussion started: 4 October 2025

Beam Width (°)	8			0.33
Pulse Length	805 ns 120.7 m	2800 ns 419.7 m	400 ns 60 m	480 ns 72.14 m
Range (m)	270– 4970	860 – 14960	150 – 10000	160 – 18010
Range Resolution (m)	50	50	50	30
Inter Pulse Period (IPP) (ms)	40	120	80	360
Pulse Repetition Frequency (PRF) (kHz)	25	8.3	12.5	2.77
Number of coherent averages	32	4	5	0
Number of Incoherent (spectral) averages	11	10	5	18
Number of FFT points	512	512	1024	256
Time Resolution including delays (sec)	9.2	4.5	4	4
Nyquist Velocity (m s^{-1})	45.2	120.5	145	6
Velocity Resolution (m s^{-1})	0.17	0.46	0.28	0.04
Beam elevation (°)	74.5 for oblique modes; 90 for vertical	90	90	90
Beam azimuth (°)	210 and 300 for oblique modes	-	-	-

In this study, we exclusively examine measurements from the vertically-pointing wind mode and the 2 precipitation modes.

https://doi.org/10.5194/egusphere-2025-4434
Preprint. Discussion started: 4 October 2025

2.2 KAZRARSCL

The Ka-band zenith ARM radar (KAZR) is a co-located zenith-pointing Doppler cloud radar that has seen a continuous presence at ENA from July 2015 to the present day (Hardin et al., 2011). The radar operates at a frequency of 34.86 GHz and can observe clouds and precipitation in the boundary layer. KAZR also operates in two modes, general mode and moderate sensitivity mode. The KAZR data is calibrated using a corner reflector. The data from the two KAZR modes is merged and noise-filtered using the technique proposed in Clothiaux et al., 2000, prior to deriving cloud boundaries. The calibrated and noise-filtered estimates of KAZR reported moments are available in the Active Remote Sensing of CLouds (ARSCL) data product.

2.3 Surface disdrometer

To calibrate the RWP, an independent surface observation is required. Following previous methodologies (Tridon et al., 2013; Williams et al., 2023), a co-located surface disdrometer has been used to calculate the equivalent reflectivity based on surface precipitation measurements. In this study, measurements from ENA's laser disdrometer (LDIS) have been used for this purpose. This LDIS, an OTT Parsivel2 manufactured by OTT Hydromet GmbH, has been in operation at ENA since February 2014. It operates by recording the shadowing effect produced by precipitation particles falling through a flat, horizontal 650 nm laser (Wang and Bartholomew, 2023). From the shadowing effect, the drop's size and fall speed are measured, and the drop is subsequently categorized into 1 of 32 bins based on its size and velocity.

While the instrument is indicated to measure drops with diameters between 0.062 mm and 24.5 mm (Wang and Bartholomew, 2023), drop number underestimations seem to be present in instances where mean hourly rain rates exceed 2.5 mm h^{-1} (Tokay et al., 2013). In the Laser Disdrometer Quantities (LDQUANTS) VAP (Hardin et al., 2020), these uncertainties are used to filter the observations, which are then binned into 1-minute temporal resolution drop size distributions (DSDs) and mean rainfall rates. These DSD observations are used to estimate equivalent reflectivity measurements using the T-matrix method (e.g. Leinonen, 2014), an output that is provided in the LDQUANTS VAP.

https://doi.org/10.5194/egusphere-2025-4434
Preprint. Discussion started: 4 October 2025

2.4 Eddy correlation flux measurement system

To isolate the effect of island heating on air motions aloft, sensible heat flux (SHF) from the eddy correlation (ECOR) flux measurement system was used (Sullivan et al., 1997). Utilizing a sonic anemometer and 2 infrared gas sensors, this system provides in situ measurements of turbulent fluxes at ENA (Cook, 2018) at a 30 minute temporal resolution.

3 RWP calibration, sensitivity and performance

In this section, the data processing of RWP moments and the calibration technique are described. Then, the application of the calibration is shown, and the sensitivity of the instrument is explored.

3.1 Noise filtering and binning

Before calibrating the radar for reflectivity, daily profiles of RWP-measured signal-to-noise ratio (SNR) were noise-filtered and binned to a uniform time resolution. The noise filtering procedure first required the identification of a noise floor, which was qualitatively assessed based on visual inspection of clear-air SNR measurements throughout the domain. During the climatology, this noise floor changed twice (Figure 2): first on April 21, 2015, likely due to a change in radar operating parameters, and again after the hardware replacement and instrument restart on September 14th, 2020. After finding these noise floors, the data is processed through a high-pass filter, wherein all pixels below this noise floor are masked out. A pixel filter is then implemented, removing any remaining noise pixels while retaining a broad dynamic range of signals. As mentioned above, the instrument was non-operational for a period in 2019 and 2020. This discontinuity can be seen in the shaded region of Figure 2 and elsewhere.

https://doi.org/10.5194/egusphere-2025-4434
Preprint. Discussion started: 4 October 2025

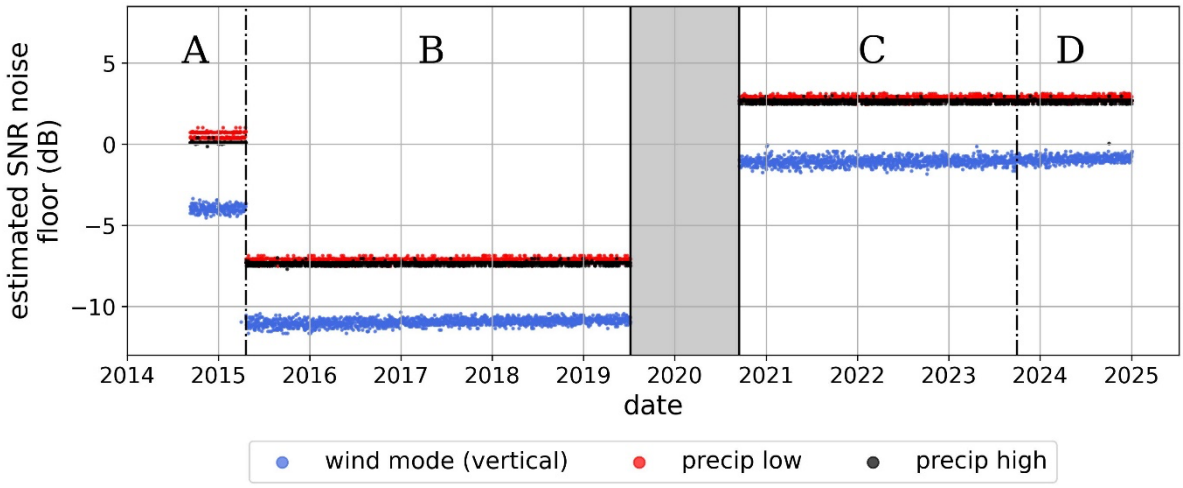

Figure 2 Derived noise floor for the vertical wind mode (blue), the short-pulse precipitation mode (red), and the long-pulse precipitation mode (black). Data epochs are labelled A, B, C, and D. Details on these epochs can be found in Table 2

Additionally, a persistent artifact of high SNR centered around 1270 m has been found during our analysis of the wind mode. Likely stemming from ground clutter present in a side lobe, this artifact is mostly filtered out by removing high-SNR pixels in this region that have a near-zero Doppler velocity. By filtering the data in this way, the artifact can be suppressed without removing actual measurements.

For this analysis, 4 data epochs are defined: A, B, C, and D. These are based on changes in operating parameters and drastic shifts in radar sensitivity (Section 3.3.3 Sensitivity and dynamic range of vertical wind mode and short pulse precipitation mode3). For specific information on these data epochs, see Table 2.

Table 2 Data epoch details

Epoch	Start	End	Note
A	September 10, 2014	April 21, 2015	Radar hardware #1

https://doi.org/10.5194/egusphere-2025-4434
Preprint. Discussion started: 4 October 2025

B	April 22, 2015	July 8, 2019	Radar hardware #1 (operating change)
-	July 9, 2019	September 13, 2020	Hardware failure
C	September 14, 2020	October 1, 2023	Radar hardware #2
D	October 1, 2023	January 1, 2025	Radar hardware #2 (heavily decreased sensitivity)

After the profiles have been noise-filtered, they are temporally binned to 1-minute resolution. The number of data points per bin varies based on the timing of the beam mode cycling, but it can generally be assumed that, for the wind modes, each 1-minute bin is an average of 1-2 measurements; and for the precipitation modes, each bin is an average of 3-4 measurements. Once this process is complete, the profile is then calibrated. These noise-filtering and temporal binning processes are illustrated in Figure 3a and b.

https://doi.org/10.5194/egusphere-2025-4434
Preprint. Discussion started: 4 October 2025

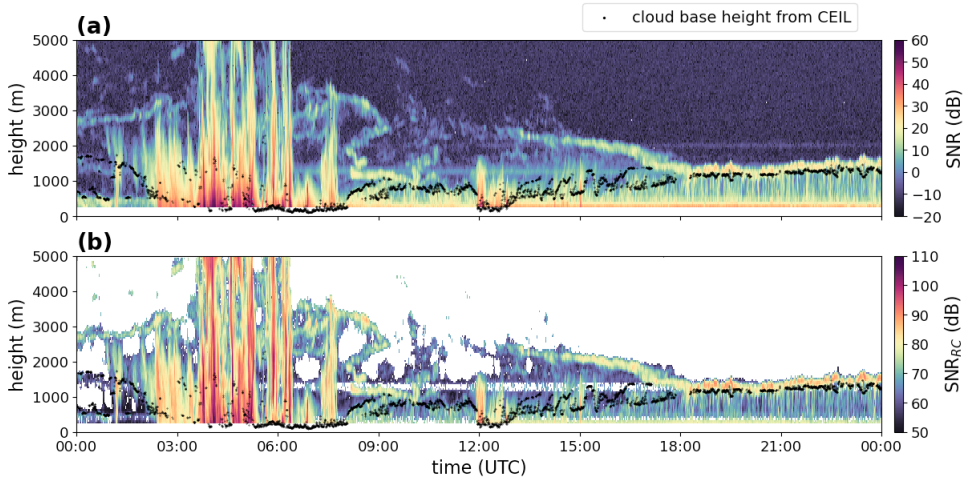

Figure 3 Example profile of vertical wind mode SNR (a) and noise-filtered and range-corrected SNR (SNR_{RC}) (b) from October 23rd, 2015.

3.2 Calibration technique

To calibrate the 1290 MHz RWP, we follow the procedure described in Tridon et al., 2013, and Williams et al., 2023. In contrast with the 915 MHz RWP used in these studies, the 1290 MHz RWP has a considerably larger Nyquist velocity (Table 1). Because of this, errors from aliasing are not a concern, and we proceed directly to calibration from disdrometer, described below.

To calculate the reflectivity from a particular beam mode, the following calculation is performed

$$Z_{beam}(r) = SNR_{beam} + 20\log(r) + C_{beam} \quad (1)$$

where r (m) is the range from the radar, SNR is the measured signal-to-noise ratio (dB), and C is the radar calibration constant. For this work, the C is calculated for two different modes: the vertically pointing wind mode and the short-pulse precipitation mode. These modes are selected because their minimum usable range gates are the closest to the surface, at 420 m for the vertical wind mode and 200 m for the short-pulse precipitation mode.

https://doi.org/10.5194/egusphere-2025-4434
Preprint. Discussion started: 4 October 2025

The lowest usable range gate for the long-pulse precipitation mode, 860 m, is too high for confident calibration with the surface disdrometer, so that mode is instead calibrated by proxy using the short-pulse precipitation mode, following Equation (***1***:

$$Z_{precip,high}(r) = SNR_{precip,high} + 20\log(r) + (C_{precip,short} - C_{precip,high}) \quad (2)$$

To calibrate the RWP, measurements from the surface disdrometer are required. Therefore, it is only possible to get a calibration constant for the 1290 MHz RWP while it is raining. Following the methodology described in Williams et al., 2023, we identify "rain events" throughout the time period, which are classified as days with at least 120 surface disdrometer observations that calculate retrievals of greater than 20 dBZ. Throughout the climatology, 949 events are identified and used for calibration at ENA. For an individual rain event day, a value of C_{beam} is calculated by taking the difference between the range-corrected SNR ($SNR_{beam} + 20\log(r)$ from Equation 1) in the lowest usable range gate for the beam mode in question and the average LDIS-measured reflectivity over the profile. Valid constants are then found by taking an average of profile C_{beam}s calculated within a 3-month period (JFM, AMJ, JAS, and OND, for each year); this average is considered the valid calibration constant for that 3-month period. Because the calibration changed significantly over time, these calibration constants had to be updated frequently and are only valid for their three-month period.

In Figure 4, an example set of calibrated RWP reflectivity profiles (Figure 4a, c, d) are shown alongside an RWP-measured wind speed profile (Figure 4b), a KAZR reflectivity profile (Figure 4e), and a time series of surface precipitation and reflectivity from LDIS (Figure 4f). The disparity between the RWP's different operational modes is immediately evident, with the wind and long pulse precipitation modes showing similar sensitivities in their measured reflectivity (albeit with the wind mode showing considerably finer vertical resolution), while the short pulse precipitation mode shows a much lower sensitivity. The air motions above cloud (Figure 4b) are strong enough to produce reflectivities on par with hydrometeors (Figure 4a), emphasizing the need for KAZR (Figure 4e) to distinguish which radar volumes are dominated by hydrometeors and which are dominated by intense air motions.

https://doi.org/10.5194/egusphere-2025-4434
Preprint. Discussion started: 4 October 2025

Additionally, when examining RWP measurements, it is useful to use the Riddle threshold (Riddle et al., 2012) to control for non-atmospheric, noisy echoes. Given the high number of calculated FFT points for this study's data (Table 1), for the vast majority of "valid" data (the definition of which is principally discussed in Section 3.3.3), RWP measurements were higher than the modes' calculated thresholds. As such, Riddle thresholding was not utilized in masking the data.

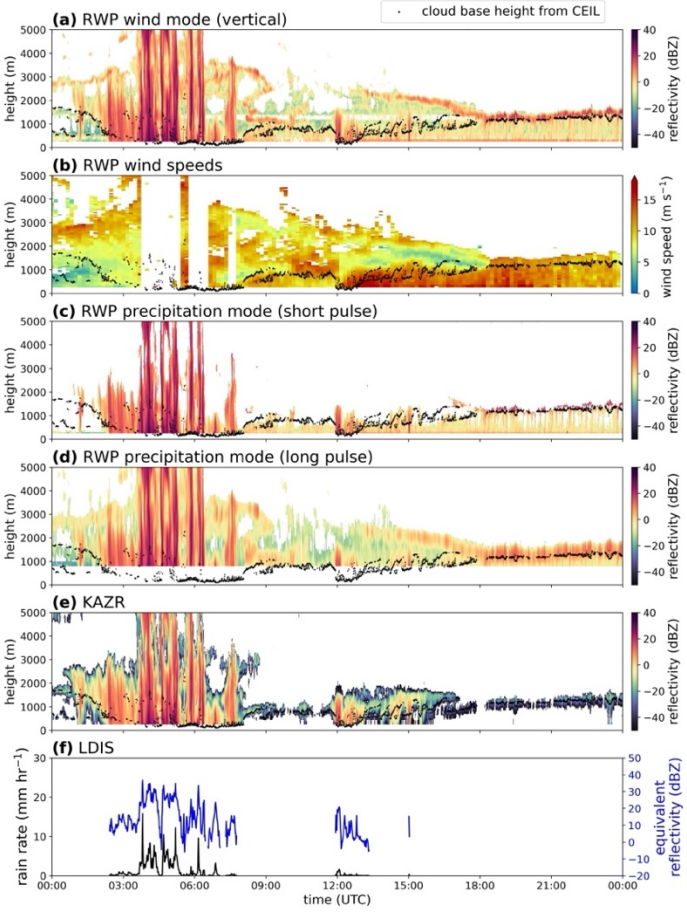

Figure 4 Example profiles of calibrated RWP vertical wind mode reflectivity (a), RWP-measured wind speeds (b), calibrated short pulse precipitation mode reflectivity (c), calibrated long pulse precipitation mode reflectivity (d), and KAZRARSCL reflectivity (e) from October 23rd, 2015. For reference, ceilometer (CEIL)-measured cloud base height is shown throughout (black dots). Also depicted are LDQUANTS retrievals of (f) rain rate (black) and reflectivity (blue) used for calibration throughout the climatology. This date was chosen for its diverse atmospheric conditions, showing the efficacy of the noise filtering and calibration in precipitating and non-precipitating regimes.

https://doi.org/10.5194/egusphere-2025-4434
Preprint. Discussion started: 4 October 2025

3.3 RWP Performance

This section shows how the calibration and sensitivity of the RWP changes over time for the duration of its operation at ENA. Following the procedure described in Section 3.2, the 1290 MHz RWP's vertical wind mode, short-pulse precipitation mode, and long pulse precipitation mode are calibrated. Subsequently, the reliability of the data is evaluated.

3.3.1 Wind mode and short pulse precipitation mode calibration

Calibration constants for the wind mode and short-pulse precipitation mode are calculated for 3-month quarters from September 10th, 2014, to January 1st, 2025 (Figure 5). During the transition period between Epoch A and Epoch B, the 2015 Q1 averaging time period is extended to include the end of the epoch: April 21, 2015. Similarly, the 2015 Q2 averaging period has been shortened to start on April 22, 2015.

https://doi.org/10.5194/egusphere-2025-4434
Preprint. Discussion started: 4 October 2025

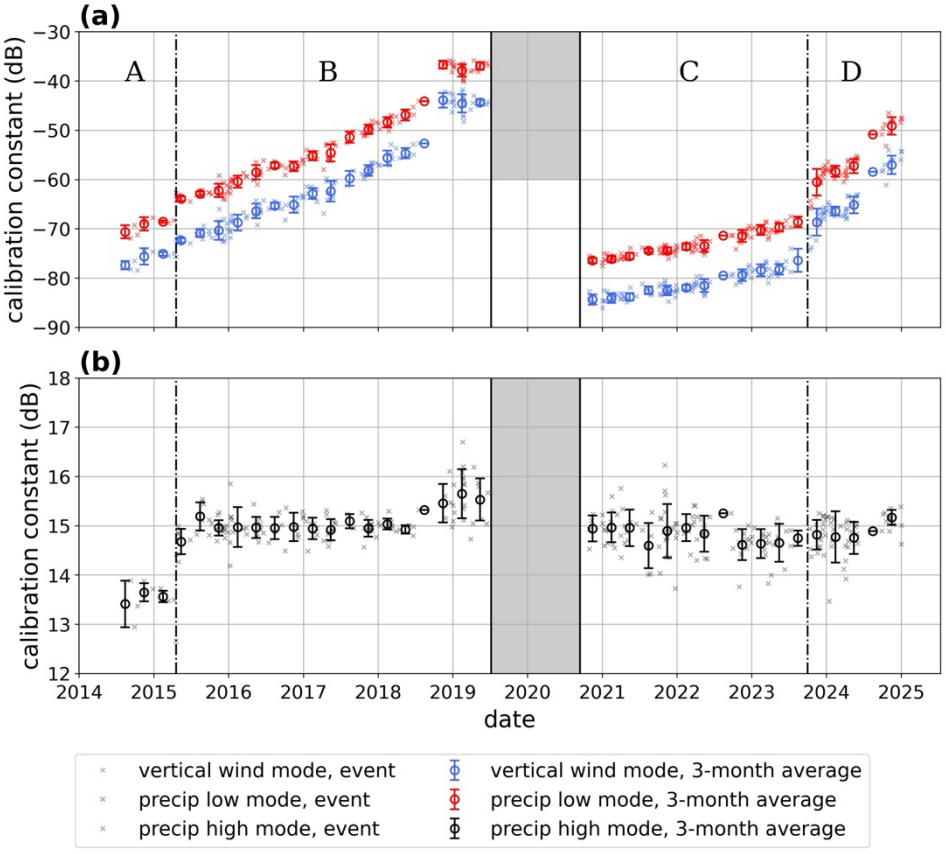

Figure 5 (a) Vertical wind mode (red) and short pulse precipitation mode (blue) calibration constants (errorbars) over time. Rain events used to calibrate the RWP (crosses, faded) are also shown. Hardware outage is greyed out. (b) Relative calibration constant for the long pulse precipitation mode (back) is shown during the same period

3.3.2 Long pulse precipitation mode calibration

As described in Section 3.2 Calibration technique, the minimum usable range gate is too high to calibrate the long pulse precipitation mode directly with the disdrometer and Equation (***2***) must be applied. The relative constant from the short pulse mode, $C_{precip,high}$, is generally found to be constant over the climatology, only seeing major shifts when the noise floor changes (Figure 5b).

https://doi.org/10.5194/egusphere-2025-4434
Preprint. Discussion started: 4 October 2025

3.3.3 Sensitivity and dynamic range of vertical wind mode and short pulse precipitation mode

The changing calibration over time seems to be indicative of some degree of decay in sensitivity. For the period before July 8, 2019, the phase shifter and antenna saw heavy corrosion, which led to the parts' replacement. It is possible something similar has occurred in the period after September 14, 2020. To better evaluate the degradation of the RWP, the sensitivity (Figure 6a) and the dynamic range (Figure 7a) have been evaluated over the instrument's lifespan at ENA.

The sensitivity of the radar has been evaluated by taking the 10^{th} percentile of the distribution of each day's radar reflectivity at 1 km. Keeping in mind that the radar reflectivity has already been noise-filtered and calibrated, this metric indicates the radar's current minimum detectable signal. Because the day-to-day 10^{th} percentile of 1-km reflectivity is noisy and heavily dependent on meteorological variability, 3-month averages of these values are calculated and are a better representation of the instrument's sensitivity for a given period. In Figure 6a, these individual cases are shown alongside the 3-month averages. Because the KAZR is used for other analysis in this work, the sensitivity in KAZRARSCL has also been evaluated (Figure 6b).

https://doi.org/10.5194/egusphere-2025-4434
Preprint. Discussion started: 4 October 2025

Looking at the RWP sensitivity plotted in Figure 6a, we see a major shift between in the slope of the change in sensitivity between Q3 and Q4 2024. This shift in sensitivity precipitated the creation of Epoch D. The epoch slopes have been found by taking a linear regression of each 3-month sensitivity mean. In, Epoch B, which runs from April 22, 2014, to July 8, 2019, RWP wind mode sensitivity steadily degrades at a rate of roughly 5.94 dBZ per year on average. The precipitation short and long pulse modes follow a similar rate, at 6.16 dBZ per year and 4.21 dBZ per year, respectively. Notably, this sensitivity degradation seems to plateau somewhat in the final months before the instrument was turned off on July 8, 2019. This "plateau" is also visible in the calibration constant (Figure 5).

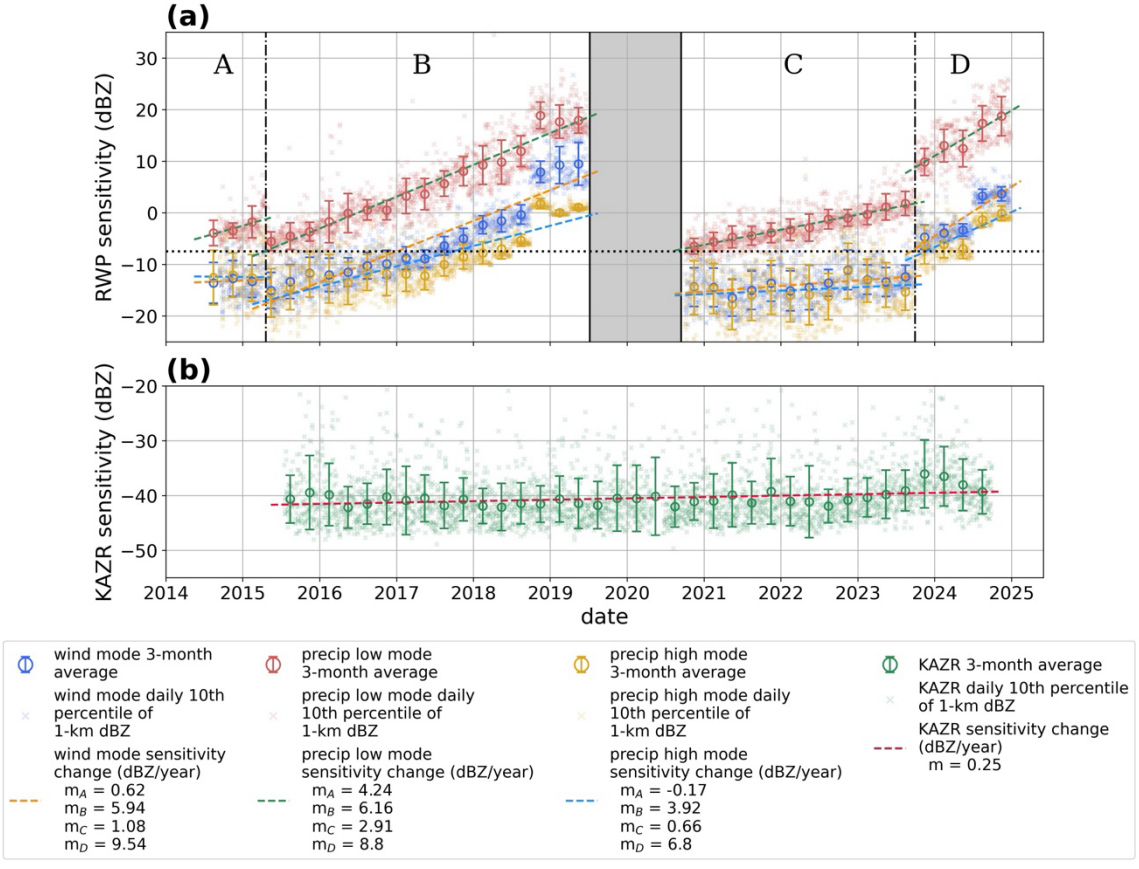

Figure 6 Sensitivity of (a) 1290 MHz RWP wind mode (blue) and (b) KAZR_ARSCL (green) over time. 3-month averages (errorbars) are shown over all daily profiles (crosses, faded).

https://doi.org/10.5194/egusphere-2025-4434
Preprint. Discussion started: 4 October 2025

After the components were replaced and the RWP returned to operation on September 14th, 2020, sensitivity degradation was distinctly slower in the wind and precipitation long-pulse modes, degrading at a rate of 1.08 dBZ per year in the wind mode and 0.49 dBZ per year in the precipitation long pulse mode until the end of September 2023 (epoch C). In the short pulse precipitation mode, however, the sensitivity degradation was much more apparent during this time period, occurring at a rate of 2.19 dBZ per year. After this point, entering epoch D, 3-month averaged radar sensitivity abruptly shifted and then began to degrade at a much faster rate of 4.82 dB per year. It is unclear what caused this enhanced sensitivity deterioration, but it has made recent profiles effectively unusable. In contrast, KAZRARSCL sensitivity (measured with the same methodology) shows a steady, slower decline of sensitivity on the order of 0.25 dB per year. Qualitatively, KAZRARSCL reflectivity profiles from 2024 do not look especially diminished from the time of the instrument's installation in 2015.

The dynamic range of the RWP and KAZRARSCL have also been evaluated (Figure 7). To estimate the dynamic range of a profile, we have taken the difference of that day's 1-km 90th percentile reflectivity and 1-km 10th percentile reflectivity. As with sensitivity, the day-to-day measurements are noisy and highly dependent on meteorology, so the per-profile dynamic ranges have been averaged over 3-month periods.

The change in average dynamic range over time in most cases follows similar trends as the sensitivity, with a more dramatic decrease in dynamic range in epoch B than C, and an abrupt, noticeable drop-off in dynamic range in epoch D. In all cases, the precipitation short-pulse mode seems to show the largest changes in sensitivity and dynamic range over time.

As with sensitivity, the KAZR shows less degradation over time, with the lowest rate of dynamic range change at -0.08 dBZ per year (Figure 7b). In comparison, it has shown itself to be a much more reliable instrument over time.

https://doi.org/10.5194/egusphere-2025-4434
Preprint. Discussion started: 4 October 2025

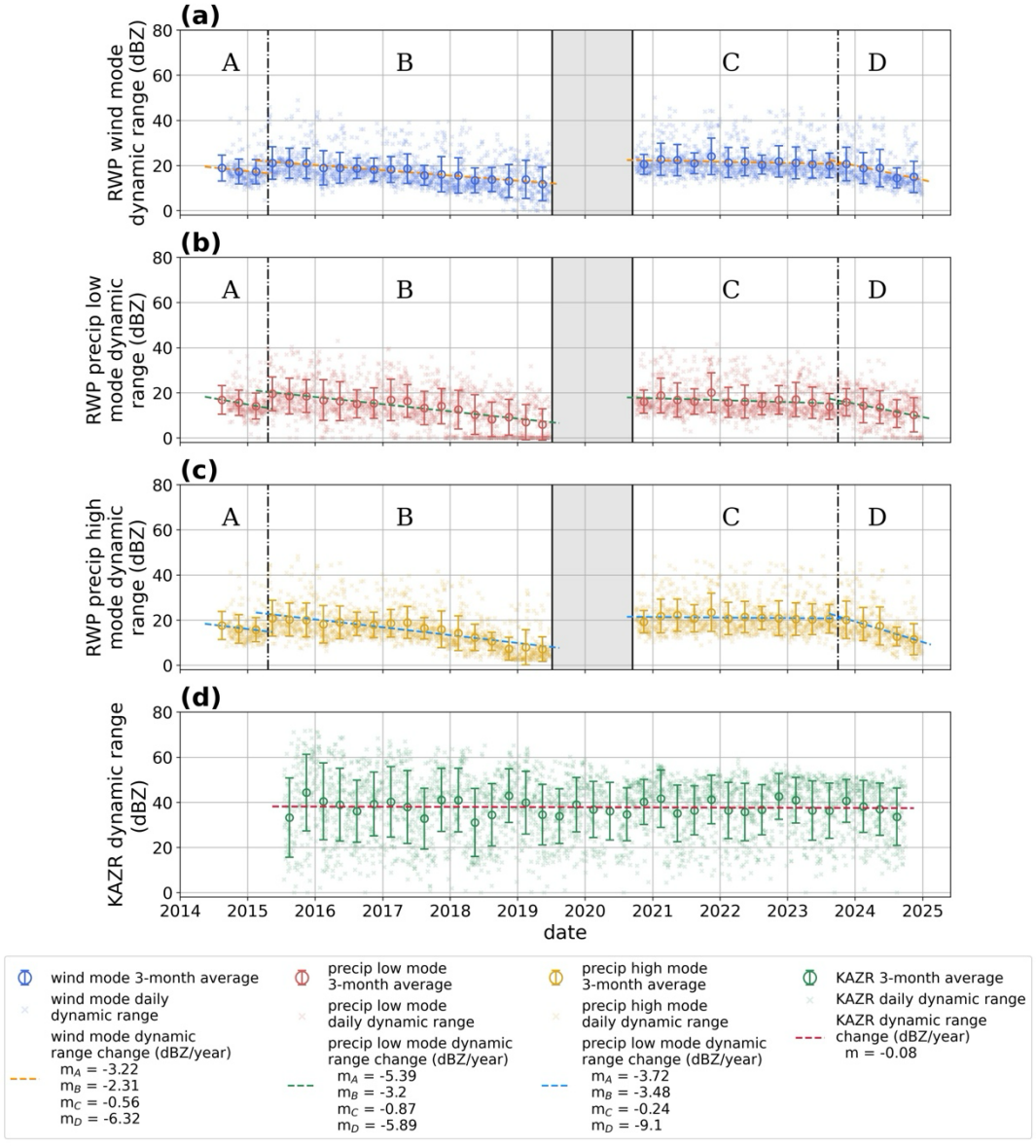

Figure 7 1-kilometer dynamic range over time in the 1290 MHz RWP (a) wind mode, (b) short pulse precipitation mode, and (c) long pulse precipitation mode. The 1-kilometer dynamic range for KAZRARSCL (e) is also shown.

One of the goals for this paper was to examine the performance of the RWP over the (current) lifetime of the dataset. It is difficult to evaluate this performance and how retrievals are affected when significant portions of the data may be degraded to the point of measurements being, at best, low

https://doi.org/10.5194/egusphere-2025-4434
Preprint. Discussion started: 4 October 2025

confidence. Therefore, it became necessary to establish a threshold with which we could delineate between "good" and "bad" RWP data. Based on the average sensitivities (Figure 6a) and qualitative assessment of the reflectivity profiles throughout the 2014-2025 climatology, we have established this threshold to be -7.5 dBZ. If the 3-month average sensitivity for a period is above the threshold -7.5 dBZ, the data from that period is considered "bad" and is not qualified for use with retrievals. This removes 39 months from the available data: July 1st, 2017, through July 8th, 2019, of Epoch B and all of Epoch D. For the following climatology measurements, any climatological or period averages are made during the remaining valid dates based on this thresholding.

4 Turbulence Retrievals

This section describes the methodology for and characteristics of retrievals of C_n^2 and ε at ENA with the 1290 MHz RWP.

4.1 Theory

Small-scale turbulent fluctuations in temperature and humidity cause changes in refractive index (Wyngaard and LeMone, 1980). These changes in the refractive index severely impact the propagation of electromagnetic waves from radar communication devices and hence need to be accurately represented in weather prediction models (Pastore et al., 2021; Wagner et al., 2016; Wang et al., 2020). These changes in the refractive index are quantified using the structure function of the refractive index (C_n^2), which can be derived from data collected by radiosonde, scintillometers, or RWP (Hegde et al., 2024; Wang et al., 2018). Here we derive C_n^2 ($m^{-2/3}$) from the calibrated reflectivity (dBZ) of the RWP using the following equation (proposed by Ralph, 1995, based off Gossard, 1988; Rogers et al., 1993) where λ is the beam wavelength in meters:

$$\log_{10} C_n^2 = \frac{dBZ}{10} - \log_{10} \lambda^{\frac{11}{3}} - 15.13 \quad (3)$$

https://doi.org/10.5194/egusphere-2025-4434
Preprint. Discussion started: 4 October 2025

Dissipation in a turbulent flow refers to the conversion of turbulence kinetic energy (TKE) to heat through molecular viscosity. It takes place at the smallest scale of the flow, known as the Kolmogorov microscale η. In classic turbulence theory (Vassilicos, 2015), ε is related to the integral length scale of the largest turbulent eddies L in the flow through

$$\varepsilon \propto \frac{e^{3/2}}{L} \tag{4}$$

where $e = \frac{1}{2}\overline{u_i u_i}$ is the TKE. The molecular dissipation happens at lengths scales order of less than 1 mm in typical atmospheric flows. As the resolution of large eddy simulation (LES) or cloud-resolving models range from 100 m to 10 km, the effect of this dissipation on the atmospheric processes need to be parameterized using higher order TKE closure schemes (Lv et al., 2023). The integral length scale (L) and the dissipation rates are known to vary with atmospheric stability, and whether the turbulence in the boundary layer is forced by wind shear or buoyancy (Akinlabi et al., 2019). The TKE dissipation rates can be derived from high resolution vertical air motion estimates from surface anemometers and those from vertically pointing Doppler lidar (Bodini et al., 2018). It can also be derived from the estimates of spectrum width from vertically pointing cloud radar (Albrecht et al., 2016; Borque et al., 2016; Fang et al., 2014). Here we use the spectrum width reported by the RWP to derive TKE dissipation rates following the methodology described by White et al., 1999, and McCaffrey et al., 2017. The RWP reported width of the Doppler spectra (σ_m) has contributions from broadening due to wind shear (σ_s), and turbulence (σ_t):

$$\sigma_m^2 = \sigma_s^2 + \sigma_t^2 \tag{5}$$

The beam broadening due to wind shear is a function of half-power beam width of the radar antenna (ν), transverse wind across the antenna (V_T), the mean wind shear ($\frac{\partial u}{\partial z}$), and the radar range resolution (ΔR).

$$\sigma_s^2 = \frac{\nu^2}{3}\left(V_T^2 + \left(\frac{\partial u}{\partial z}\right)^2 \frac{\Delta R^2}{12}\right) \tag{6}$$

https://doi.org/10.5194/egusphere-2025-4434
Preprint. Discussion started: 4 October 2025

Hence, the contribution of turbulence to the measured width of the Doppler spectra can be calculated by subtracting the contribution from wind shear. The consensus winds reported by the RWP (Muradyan and Ermold, 2021a) were used for V_T in equation (6 and following. White et al., 1999, reported the following equation relating the contribution of turbulence to spectrum width and TKE dissipation rate in a spherical coordinate system

$$\sigma_t^2 = \frac{\alpha \varepsilon^{2/3}}{4\pi}\left[12\Gamma\left(\frac{2}{3}\right)\int_0^{\pi/2} d\phi \int_0^{\pi/2} d\theta \sin^3\theta \left(b^2\cos^2\theta + a^2\sin^2\theta + \frac{L}{12}\sin^2\theta\cos^2\phi\right)^{1/3}\right] \quad (7)$$

where $\alpha = 1.6$ is the Kolmogorov constant, $L = V_T \Delta t$ where Δt is the dwell time (s), a is the half-diameter of the beam cross-section (m), b is the half-length of the pulse (m), and Γ is the gamma function. The above equation is numerically integrated and then solved for the TKE dissipation rate (ε).

As clouds and precipitation are known to increase the RWP reflectivity due to Rayleigh scattering and affect the spectrum width, the C_n^2 and ε retrievals are only made in regions devoid of any hydrometeors. This methodology is described in further detail in Section 4.2.

4.2 Measurements

C_n^2 and ε were calculated as described in Section 4.1 Theory across the entire valid climatology (Section 3.3.3 Sensitivity and dynamic range of vertical wind mode and short pulse precipitation mode).

https://doi.org/10.5194/egusphere-2025-4434
Preprint. Discussion started: 4 October 2025

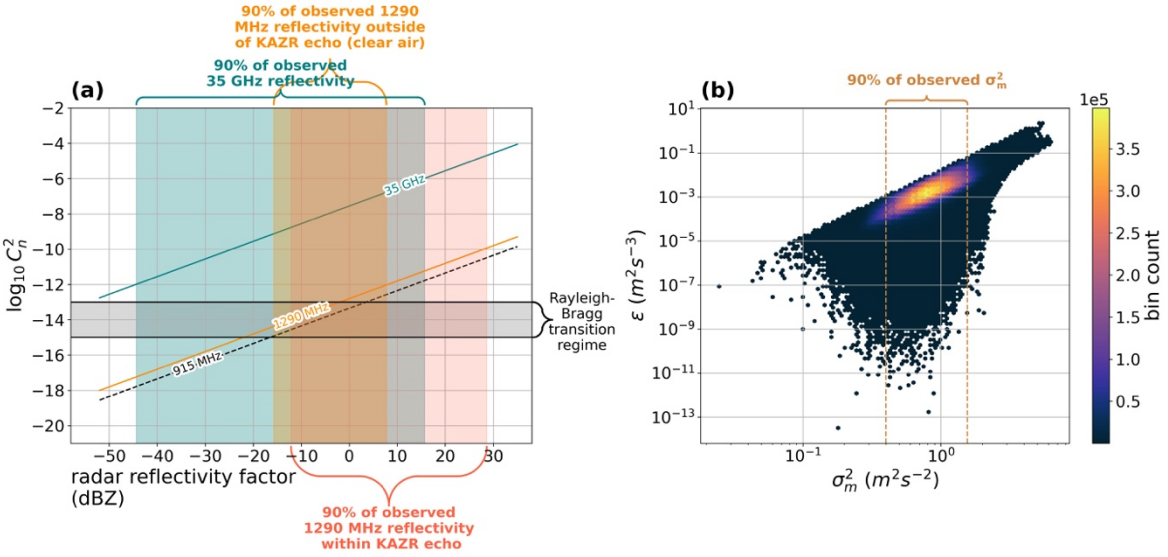

Figure 8 (a) Measured C_n^2 for the 1290 MHz RWP within KAZRARSCL echo boundaries (gold shaded region), for the 1290 MHz RWP outside of KAZRARSCL echo boundaries (salmon shaded region), and for the 35 GHz KAZRARSCL dataset (turquoise shaded region). The Rayleigh-Bragg transition regime (grey shaded region), defined in Ralph, 1995, is also depicted. (b) Measured σ_m^2 versus ε across the dataset is also depicted. σ_t^2 and ε have a log-linear relationship, varied somewhat by wind shear.

We've observed that, at ENA, a significant portion of measured C_n^2 is higher than what Ralph, 1995, describes as the Rayleigh-Bragg transition regime. For values of C_n^2 below this regime (i.e. values lower than 10^{-15} $m^{-2/3}$), Bragg scattering from clear-air measurements typically dominates, and for values above this regime (i.e. values higher than 10^{-13} $m^{-2/3}$), Rayleigh scattering typically dominates. To control for this and retrieve clear-air motions in high C_n^2 regions, we have used the reflectivity from the KAZRARSCL VAP (processed from the co-located KAZR) to distinguish regions containing hydrometeors in the RWP reflectivity profiles. To reinforce this point, the distribution of a KAZR-equivalent C_n^2 is provided (Figure 8a), remaining entirely in the Rayleigh-dominated regime. We find that 90% of measured clear-air C_n^2 is between 10^{-15} $m^{2/3}$ and 10^{-13} $m^{2/3}$, highlighting the need for this additional KAZR-masking methodology. These values broadly align with prior studies examining C_n^2 in the boundary layer (Hartten et al., 2019; Hartten and Johnston, 2014; Nath et al., 2010).

ε is generally proportional to σ_m^2 (Figure 8b) and in turn σ_t^2. Throughout the climatology, there are instances where negative values of σ_t^2 are recorded. This occurs in cases where the shear and beam-

https://doi.org/10.5194/egusphere-2025-4434
Preprint. Discussion started: 4 October 2025

broadening term, σ_s^2, is greater than the measured spectral width, σ_m^2. This result occurs in 2.091% of cases across the scope of valid measurements (Figure 9a) and tends to scale with height (Figure 9b). This compares well with McCaffrey et al., 2017, which sees a similar increase with height of $\sigma_m^2 < \sigma_s^2$ for a 915 MHz RWP, albeit at a higher rate (around 25% of the time through the vertical profile). Ultimately, these negative σ_t^2 are not physically meaningful and are subsequently discarded for any further analysis.

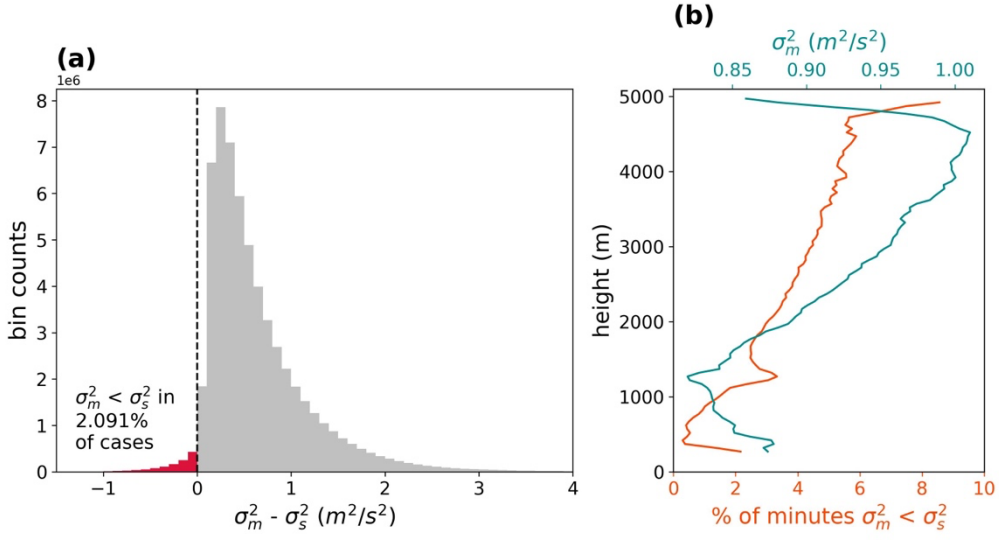

Figure 9 (a) A histogram of σ_m^2 - σ_s^2 across the dataset, with valid (positive) measurements colored in grey and invalid (negative) values colored in red. A negative measurement is made 2.091% of the time. (b) Percentage of the time $\sigma_m^2 < \sigma_s^2$ with height (orange) and σ_m^2 with height (cyan), averaged over the dataset.

Generally, we see that σ_t^2 is a strong controller of σ_m^2 (Figure 9b). While there is a relatively high rate of $\sigma_m^2 < \sigma_s^2$ in the first three range gates (270 m – 370 m), this is largely due to high noise in these range gates. The "spike" in $\sigma_m^2 < \sigma_s^2$ at 1270 m can be primarily attributed to a persistent artifact occurring around this range gate (discussed in Section 3.1 Noise filtering and binning, visually identifiable in Figure 3) that was not perfectly filtered.

https://doi.org/10.5194/egusphere-2025-4434
Preprint. Discussion started: 4 October 2025

5 Climatology

Prevailing winds observed by the 1290 MHz RWP at ENA tend to be from the southwest (Figure 1) and are generally governed, like most of the Açores' meteorology, by the shifting Açores high and the Icelandic low (commonly called the North Atlantic Oscillation) (Wang et al., 2022; Wood et al., 2015). While the Açores high is always present in the North Atlantic, its center shifts seasonally, from a position to the southwest of the archipelago in the summer to directly overhead in the winter (Wang et al., 2022). As it does this, the Icelandic low deepens and the cyclone track moves north, bringing the Açores into the trajectory of many extratropical cyclones moving westward across the Atlantic (Rémillard and Tselioudis, 2015; Wang et al., 2022). This annual movement of the Açores high is the likely driver behind the observed seasonal shift in the winds from a wider spread between 210° and 360° (Figure 10b-d) during most of the year to a mainly westerly flow between 210° and 290° (Figure 10a).

In Rémillard and Tselioudis, 2015, it was shown that 850-hPa winds during storms are dominated by west-southwesterly flow, while out-of-storm winds tend to come from a broader, west-to-northwesterly direction. This aligns well with the observations aloft (~1500m) in this work, which show a more broad west-to-northwesterly flow in all seasons but DJF, when ENA is more strongly influenced by extratropical cyclones (Rémillard and Tselioudis, 2015).

https://doi.org/10.5194/egusphere-2025-4434
Preprint. Discussion started: 4 October 2025

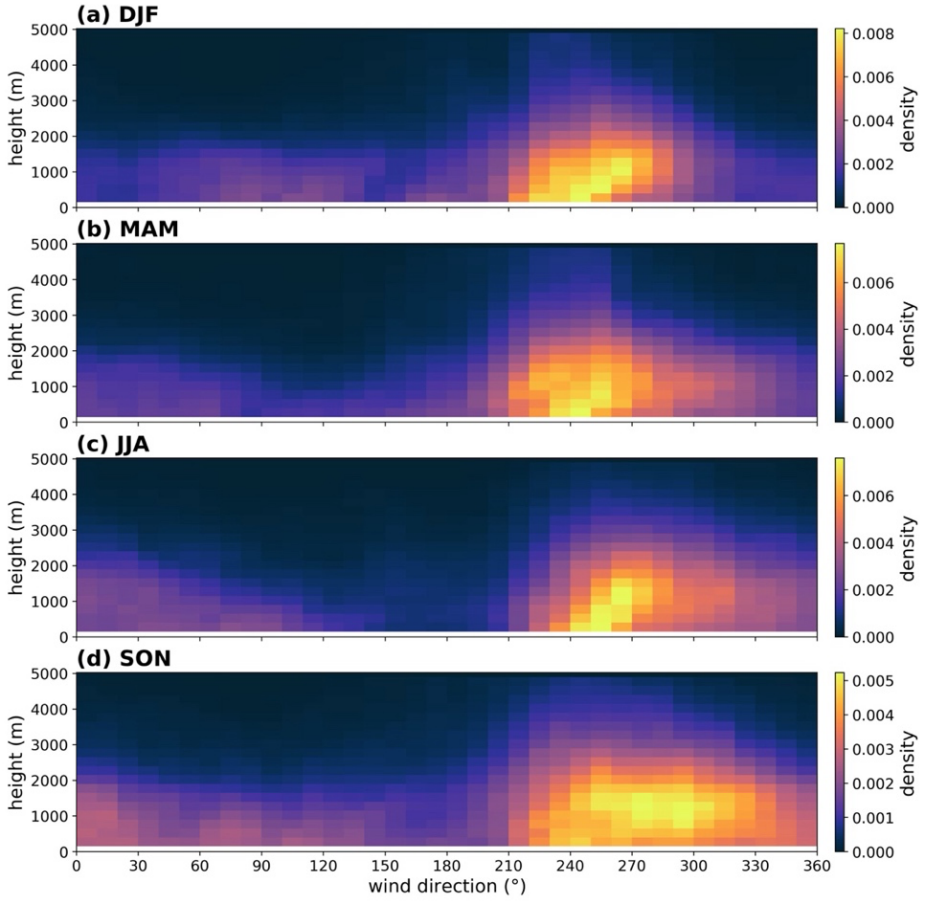

Figure 10 Seasonal frequency of wind direction across height for DJF (a), MAM (b), JJA (c), and SON (d) as observed by the 1290 MHz RWP.

One of the key uses of observations from ENA is increasing our understanding of the conditions in the marine boundary layer. Because of this, it is useful to isolate observations that are coming purely from the ocean, especially when we consider contrasting ESMs with observations from ENA. Because islands in the Açores are not large enough to be represented in ESMs operating at global resolutions, local island effects are not represented. In the real world, the predominant southwesterly winds pass over several miles of Graciosa Island before coming into the view of the vertically-pointing instruments used in this study and are influenced by local island meteorology. Further south, larger and taller islands in the chain may be similarly affecting the aerosol and cloud conditions observed at ENA.

https://doi.org/10.5194/egusphere-2025-4434
Preprint. Discussion started: 4 October 2025

410

To examine this effect, it is useful to look at the diurnal cycle of ε on days when updrafts are expected. For this, observations of ε at 520 m have been subset to only hours where ENA ECOR recorded SHF of 20 W m^{-2} or higher and then averaged across the domain. Following the methodology described in Ghate et al., 2021, we describe "marine" winds as coming from directions between 310° and 90°. Winds coming from all other directions are considered "island" winds. In Figure 11, we see that there is on average higher ε aloft during conditions where wind is coming from island directions, indicating an island influence on the air coming from these directions.

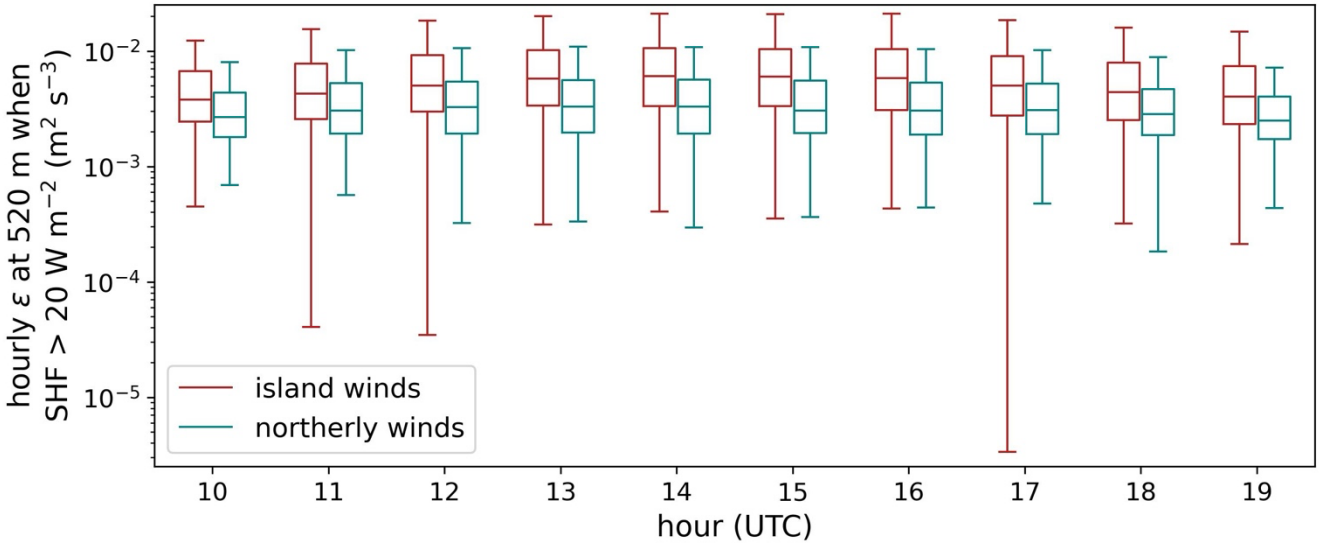

Figure 11 Diurnal ε at 520 m when SHF > 20 W m^{-2} is measured by ECOR. Because the majority of observations occur during daylight hours, the data has been subset to hours 10 through 19.

420 To isolate our observations from these effects and produce observations that may be compared with ESM output, it is useful to divide observations between island and marine conditions. Because the marine winds are more directly from the ocean and crossing much less of the island, we can be confident that they are representative of marine conditions and, subsequently, the typical ESM gridcell for this region. These northerly flow conditions are only present ~30% of the time and most commonly observed 425 in SON (Ghate et al., 2021).

https://doi.org/10.5194/egusphere-2025-4434
Preprint. Discussion started: 4 October 2025

To characterize and explore the turbulent conditions present in the marine boundary layer at ENA (as defined by our northerly wind condition), we organize the data into monthly averaged profiles (Figure 12a-d). Before averaging into a monthly climatology, this data has been averaged to hourly temporal resolution and 150 m (3 range gates) vertical resolution to filter out noise. If a 1-hour/150-m pixel of data is not at least 80% filled with observations (in other words, is filled with more than 20% NaN), the pixel is discarded.

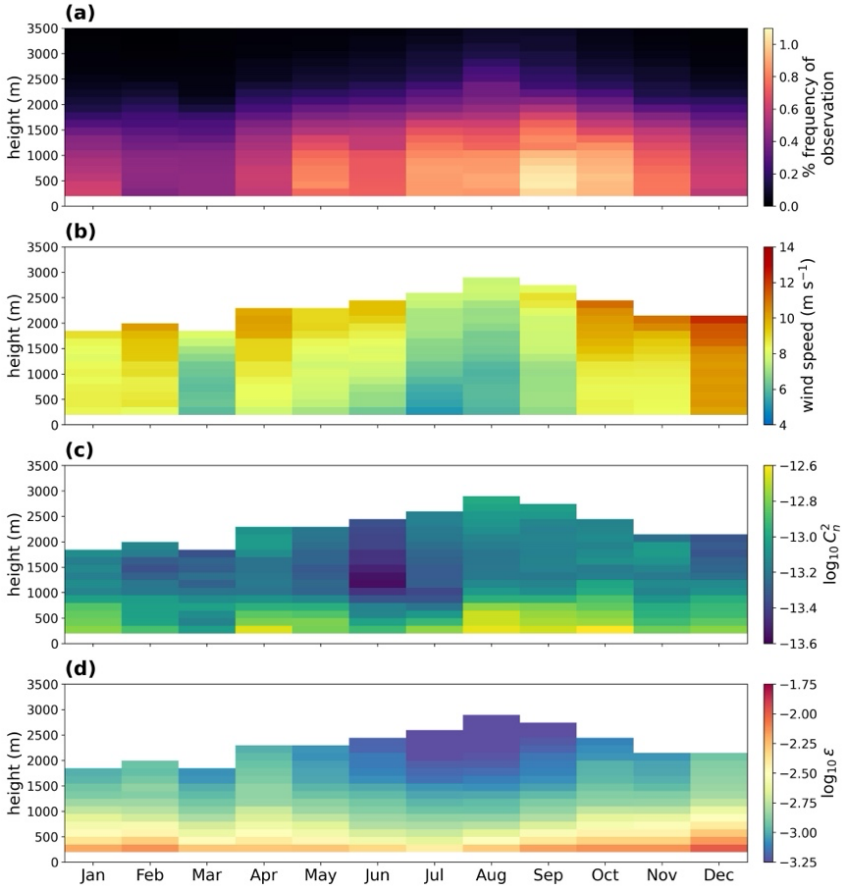

Figure 12 Month-height averages of hourly observation frequency (a), wind speed (b), ε (c), and C_n^2 (d) for northerly (marine) winds observed at ENA with the 1290 MHz RWP. For ε and C_n^2 values (c, d), the median value for each bin is used rather than the mean to accommodate for ranges that span several orders of magnitude. Bins with fewer than 200 hours of data are masked out.

https://doi.org/10.5194/egusphere-2025-4434
Preprint. Discussion started: 4 October 2025

In agreement with surface wind direction measurements described in Ghate et al., 2021, marine winds are most frequently observed in the late summer and early autumn months, with a lower frequency in the winter/spring months and a slight jump in May (Figure 12a). Average wind speeds (Figure 12b) also agreeing well with Ghate et al., 2021 and peak in the autumn and winter months, with a secondary spike in April. June and July are the calmest months at ENA with comparatively low mean winds and vertical velocities across height levels. Accordingly, they see the lowest values of C_n^2 (Figure 12c) and ε (Figure 12d).

Overall, in the late autumn and winter months ENA experiences its most intense marine-driven turbulent conditions with the strongest updrafts and highest TKE dissipation rates. In winter low pressure systems to the north-northwest of Graciosa Island drive westerly transport of moist air masses to the Açores, bringing more frontal activity from midlatitude cyclones (Dong et al., 2014; Rémillard and Tselioudis, 2015). These months also bring higher rain rates (Ghate et al., 2021), deeper PBLs (Ghate et al., 2021), and deeper clouds across precipitating and non-precipitating regimes (Rémillard and Tselioudis, 2015).

6 Summary

In this work, 9.5 years of 1290 MHz radar wind profiler data from ENA are noise filtered and calibrated. In doing so, changes to the radar sensitivity and dynamic range were evaluated over time, and a threshold for discarding degraded data was established based on measurements of the radar sensitivity at 1-km. This cut the range of usable data down from 9.5 to 6 years and we determined that the RWP at ENA is not reliable at present. Using the 6 years of vetted data, we calculated the climatology of marine wind conditions at ENA.

Agreeing with previous research performed at ENA (Rémillard and Tselioudis, 2015; Wood et al., 2015), more frequent westerly winds are observed in the winter months, with a broader spread during the rest of the year (particularly autumn). Higher wind speeds and vertical velocities are observed in the marine boundary layer during SON and DJF months, replicating results found in prior studies (Ghate et al., 2021).

https://doi.org/10.5194/egusphere-2025-4434
Preprint. Discussion started: 4 October 2025

We reported long-term statistics of C_n^2 and ε in the marine boundary layer at ENA. These high-vertical-resolution retrievals from the 1290 MHz RWP are most frequently retrieved within the first 3 km of the atmosphere and are reliably reported during 6 years of the RWP's lifetime at ENA. These results and data are relevant for ESM cloud parameterization development and parameterization evaluation. For instance, prior work (Ghate and Cadeddu, 2019) have shown that drizzle evaporation below stratocumulus clouds affects marine boundary layer (MBL) turbulence and the evolution of associated cloud properties; this link between subcloud drizzle, turbulence, and vertical mass flux may not be adequately represented by ESMs, especially in models where subgrid precipitation is diagnostic. By finely examining turbulence in domains near to drizzle, these modeled relationships may be improved.

To isolate the observations to marine conditions and remove island effects (Figure 11) we limited our climatology to observations made during marine wind conditions which are only present ~30% of the time (Figure 12). Most northerly wind conditions occur during SON and minimize in DJF. This subsetting is useful for understanding behavior over the Atlantic and making any comparison to ESMs. Along the same lines, these reported conditions are not wholly representative of overall conditions at ENA, and comparisons to ESMs will likely require some degree of seasonal weighting.

ENA is exemplary of the unique benefits that ARM observatories provide: long-running, consistent measurements of atmospheric phenomena on climatological timescales that allow for similarly-scaled scientific inquiry. The site's 1290 MHz RWP is another dimension through which much-needed analysis into properties of the MBL may be conducted, with 6 years of usable data over a variety of meteorological regimes. Despite this unique capability, at the time of writing there are few published works employing this dataset, and none utilizing measurements beyond retrieved wind speeds and directions. With the ability to observe 3-dimensional winds and turbulence above and below the cloud layer, the applications for examining turbulence, entrainment, and detrainment in and around the MBL and in a statistically-robust framework are at our fingertips. This is a goal for future work with the ENA 1290 MHz RWP and the authors encourage further usage of this dataset towards these ends.

https://doi.org/10.5194/egusphere-2025-4434
Preprint. Discussion started: 4 October 2025

Data availability

Data were obtained from the Atmospheric Radiation Measurement (ARM) user facility, a US Department of Energy (DOE) Office of Science user facility managed by the Biological and Environmental Research Program. The following data citations are provided for each ARM data product: Laser disdrometer quantities (LDQUANTS) (https://doi.org/10.5439/1432694, Hardin et al., 2019), 1290-MHz Radar Wind Profiler: Wind Moments, operating in low power mode (https://doi.org/10.5439/1663226, Muradyan and Ermold, 2021d), 1290-MHz Radar Wind Profiler: Precipitation Moments, operating in low power mode (https://doi.org/10.5439/1663225, Muradyan and Ermold, 2021c), 1290-MHz Radar Wind Profiler: Precipitation Moments, operating in high power mode (https://doi.org/10.5439/1663224, Muradyan and Ermold, 2021b), 1290-MHz Radar Wind Profiler: Low Mode Wind Averages (https://doi.org/10.5439/1663214, Muradyan and Ermold, 2021a), Active Remote Sensing of CLouds (ARSCL) product using Ka-band ARM Zenith Radars (KAZRARSCL) (https://doi.org/10.5439/1393437, Johnson et al., 2014), Eddy Correlation Flux Measurement System (ECOR) (https://doi.org/10.5439/1025039, Sullivan et al., 1997). Upon final publication, the RWP retrieval data generated from this study will be available on the ARM PI Data Archive.

Author contributions

AM and VPG participated in conceptualization, methodology, formal analysis, and writing (original draft preparation). AM performed visualization, and data curation. VPG and DTM provided project administration and resources. VPG, DTM, and HG contributed to funding acquisition. All authors contributed to the review and editing process.

Competing interests

The authors declare that they have no conflict of interest.

Acknowledgements

We would like to acknowledge the use of computational resources (doi:10.5065/D6RX99HX) at the NCAR-Wyoming Supercomputing Center provided by the National Science Foundation and the State of Wyoming and supported by NCAR's Computational and Information Systems Laboratory. Special thanks to Maria P. Cadeddu for her work on an earlier version of this project and her helpful comments in the editing this manuscript.

Financial support

AM, HG, and DTM were supported by the U.S. Department of Energy's Atmospheric System Research Federal Award DE-SC0022227. VPG was supported by the U.S. Department of Energy's Atmospheric System Research, an Office of Science,

https://doi.org/10.5194/egusphere-2025-4434
Preprint. Discussion started: 4 October 2025

Office of Biological and Environmental Research program, under Contract DE-AC02-06CH11357 awarded to Argonne National Laboratory. This research made possible through a partnership between the University of Wyoming School of Computing and Argonne National Laboratory.

References

Akinlabi, E. O., Wacławczyk, M., Mellado, J. P., and Malinowski, S. P.: Estimating Turbulence Kinetic Energy Dissipation Rates in the Numerically Simulated Stratocumulus Cloud-Top Mixing Layer: Evaluation of Different Methods, Journal of the Atmospheric Sciences, 76, 1471–1488, https://doi.org/10.1175/JAS-D-18-0146.1, 2019.

Albrecht, B., Fang, M., and Ghate, V.: Exploring Stratocumulus Cloud-Top Entrainment Processes and Parameterizations by Using Doppler Cloud Radar Observations, Journal of the Atmospheric Sciences, 73, 729–742, https://doi.org/10.1175/JAS-D-15-0147.1, 2016.

Bianco, L., Wilczak, J. M., and White, A. B.: Convective Boundary Layer Depth Estimation from Wind Profilers: Statistical Comparison between an Automated Algorithm and Expert Estimations, Journal of Atmospheric and Oceanic Technology, 25, 1397–1413, https://doi.org/10.1175/2008JTECHA981.1, 2008.

Bodini, N., Lundquist, J. K., and Newsom, R. K.: Estimation of turbulence dissipation rate and its variability from sonic anemometer and wind Doppler lidar during the XPIA field campaign, Atmospheric Measurement Techniques, 11, 4291–4308, https://doi.org/10.5194/amt-11-4291-2018, 2018.

Borque, P., Luke, E., and Kollias, P.: On the unified estimation of turbulence eddy dissipation rate using Doppler cloud radars and lidars, Journal of Geophysical Research: Atmospheres, 121, 5972–5989, https://doi.org/10.1002/2015JD024543, 2016.

Clothiaux, E. E., Ackerman, T. P., Mace, G. G., Moran, K. P., Marchand, R. T., Miller, M. A., and Martner, B. E.: Objective Determination of Cloud Heights and Radar Reflectivities Using a Combination of Active Remote Sensors at the ARM CART Sites, Journal of Applied Meteorology and Climatology, 39, 645–665, https://doi.org/10.1175/1520-0450(2000)039<0645:ODOCHA>2.0.CO;2, 2000.

Cook, D. R.: Eddy Correlation Flux Measurement System (ECOR) Instrument Handbook, ARM user facility, Pacific Northwest National Laboratory, Richland, WA, https://doi.org/10.2172/1467448, 2018.

Dong, X., Xi, B., Kennedy, A., Minnis, P., and Wood, R.: A 19-Month Record of Marine Aerosol–Cloud–Radiation Properties Derived from DOE ARM Mobile Facility Deployment at the Azores. Part I: Cloud Fraction and Single-Layered MBL Cloud Properties, Journal of Climate, 27, 3665–3682, https://doi.org/10.1175/JCLI-D-13-00553.1, 2014.

Fang, M., Albrecht, B. A., Ghate, V. P., and Kollias, P.: Turbulence in Continental Stratocumulus, Part I: External Forcings and Turbulence Structures, Boundary-Layer Meteorol, 150, 341–360, https://doi.org/10.1007/s10546-013-9873-3, 2014.

Ghate, V. P. and Cadeddu, M. P.: Drizzle and Turbulence Below Closed Cellular Marine Stratocumulus Clouds, Journal of Geophysical Research: Atmospheres, 124, 5724–5737, https://doi.org/10.1029/2018JD030141, 2019.

Ghate, V. P., Cadeddu, M. P., Zheng, X., and O'Connor, E.: Turbulence in the Marine Boundary Layer and Air Motions below Stratocumulus Clouds at the ARM Eastern North Atlantic Site, Journal of Applied Meteorology and Climatology, 60, 1495–1510, https://doi.org/10.1175/JAMC-D-21-0087.1, 2021.

https://doi.org/10.5194/egusphere-2025-4434
Preprint. Discussion started: 4 October 2025

Ghate, V. P., Surleta, T., Magaritz-Ronen, L., Raveh-Rubin, S., Gallo, F., Carlton, A. G., and Azevedo, E. B.: Drivers of Cloud Condensation Nuclei in the Eastern North Atlantic as Observed at the ARM Site, Journal of Geophysical Research: Atmospheres, 128, e2023JD038636, https://doi.org/10.1029/2023JD038636, 2023.

Gossard, E. E.: Measuring Drop-Size Distributions in Clouds with a Clear-Air-Sensing Doppler Radar, Journal of Atmospheric and Oceanic Technology, 5, 640–649, https://doi.org/10.1175/1520-0426(1988)005<0640:MDSDIC>2.0.CO;2, 1988.

Gossard, E. E., Wolfe, D. E., Moran, K. P., Paulus, R. A., Anderson, K. D., and Rogers, L. T.: Measurement of Clear-Air Gradients and Turbulence Properties with Radar Wind Profilers, Journal of Atmospheric and Oceanic Technology, 15, 321–342, https://doi.org/10.1175/1520-0426(1998)015<0321:MOCAGA>2.0.CO;2, 1998.

Hardin, J., Nelson, D., Lindenmaier, I., Isom, B., Johnson, K., Matthews, A., and Bharadwaj, N.: ARM: Ka ARM Zenith Radar (KAZR): general mode, Oak Ridge National Lab. (ORNL), Oak Ridge, TN (United States). Atmospheric Radiation Measurement (ARM) Archive, https://doi.org/10.5439/1025214, 2011.

Hardin, J., Giangrande, S., and Zhou, A.: ldquants, Atmospheric Radiation Measurement (ARM) Archive, Oak Ridge National Laboratory (ORNL), Oak Ridge, TN (US); ARM Data Center, Oak Ridge National Laboratory (ORNL), Oak Ridge, TN (United States), https://doi.org/10.5439/1432694, 2019.

Hardin, J., Giangrande, S. E., and Zhou, A.: Laser Disdrometer Quantities (LDQUANTS) and Video Disdrometer Quantities (VDISQUANTS) Value-Added Products Report, ARM user facility, Pacific Northwest National Laboratory, Richland, WA, United States, https://doi.org/10.2172/1808573, 2020.

Hartmann, D. L. and Short, D. A.: On the Use of Earth Radiation Budget Statistics for Studies of Clouds and Climate, Journal of the Atmospheric Sciences, 37, 1233–1250, https://doi.org/10.1175/1520-0469(1980)037<1233:OTUOER>2.0.CO;2, 1980.

Hartten, L. M. and Johnston, P. E.: Stratocumulus-Topped Marine Boundary Layer Processes Revealed by the Absence of Profiler Reflectivity, Journal of Applied Meteorology and Climatology, 53, 1775–1789, https://doi.org/10.1175/JAMC-D-12-0308.1, 2014.

Hartten, L. M., Johnston, P. E., Castro, V. M. R., and Pérez, P. S. E.: Postdeployment Calibration of a Tropical UHF Profiling Radar via Surface- and Satellite-Based Methods, Journal of Atmospheric and Oceanic Technology, 36, 1729–1751, https://doi.org/10.1175/JTECH-D-18-0020.1, 2019.

Hegde, R., Anand, N., Satheesh, S. K., and Moorthy, K. K.: Modeling the atmospheric refractive index structure parameter using macrometeorological observations, Appl. Opt., AO, 63, E10–E17, https://doi.org/10.1364/AO.519025, 2024.

Johnson, K., Giangrande, S., and Toto, T.: KAZRARSCL-c0-All-inclusive data stream, Oak Ridge National Lab. (ORNL), Oak Ridge, TN (United States). Atmospheric Radiation Measurement (ARM) Archive; Oak Ridge National Lab. (ORNL), Oak Ridge, TN (United States). Atmospheric Radiation Measurement (ARM) Data Center, https://doi.org/10.5439/1393437, 2014.

Leinonen, J.: High-level interface to T-matrix scattering calculations: architecture, capabilities and limitations, Opt. Express, OE, 22, 1655–1660, https://doi.org/10.1364/OE.22.001655, 2014.

Lv, Y., Muñoz-Esparza, D., Chen, X., Zhang, C., Luo, M., Wang, R., and Zhou, B.: Stability Dependence of the Turbulent Dissipation Rate in the Convective Atmospheric Boundary Layer, Geophysical Research Letters, 50, e2023GL103326, https://doi.org/10.1029/2023GL103326, 2023.

https://doi.org/10.5194/egusphere-2025-4434
Preprint. Discussion started: 4 October 2025

Mather, J. H. and Voyles, J. W.: The Arm Climate Research Facility: A Review of Structure and Capabilities, Bulletin of the American Meteorological Society, 94, 377–392, https://doi.org/10.1175/BAMS-D-11-00218.1, 2013.

McCaffrey, K., Bianco, L., and Wilczak, J. M.: Improved observations of turbulence dissipation rates from wind profiling radars, Atmos. Meas. Tech., 10, 2595–2611, https://doi.org/10.5194/amt-10-2595-2017, 2017.

Molod, A., Takacs, L., Suarez, M., and Bacmeister, J.: Development of the GEOS-5 atmospheric general circulation model: evolution from MERRA to MERRA2, Geoscientific Model Development, 8, 1339–1356, https://doi.org/10.5194/gmd-8-1339-2015, 2015.

Muradyan, P. and Coulter, R.: Radar Wind Profiler (RWP) and Radio Acoustic Sounding System (RASS) Instrument Handbook, PNNL; Richland, WA, https://doi.org/10.2172/1020560, 2020.

Muradyan, P. and Ermold, B.: 1290-MHz Radar Wind Profiler: Low Mode Wind Averages, Oak Ridge National Lab. (ORNL), Oak Ridge, TN (United States). Atmospheric Radiation Measurement (ARM) Archive; Oak Ridge National Lab. (ORNL), Oak Ridge, TN (United States). Atmospheric Radiation Measurement (ARM) Data Center, https://doi.org/10.5439/1663214, 2021a.

Muradyan, P. and Ermold, B.: 1290-MHz Radar Wind Profiler: Precipitation Moments, operating in high power mode, Oak Ridge National Lab. (ORNL), Oak Ridge, TN (United States). Atmospheric Radiation Measurement (ARM) Archive; Oak Ridge National Lab. (ORNL), Oak Ridge, TN (United States). Atmospheric Radiation Measurement (ARM) Data Center, https://doi.org/10.5439/1663224, 2021b.

Muradyan, P. and Ermold, B.: 1290-MHz Radar Wind Profiler: Precipitation Moments, operating in low power mode, Oak Ridge National Lab. (ORNL), Oak Ridge, TN (United States). Atmospheric Radiation Measurement (ARM) Archive; Oak Ridge National Lab. (ORNL), Oak Ridge, TN (United States). Atmospheric Radiation Measurement (ARM) Data Center, https://doi.org/10.5439/1663225, 2021c.

Muradyan, P. and Ermold, B.: 1290-MHz Radar Wind Profiler: Wind Moments, operating in low power mode, Oak Ridge National Lab. (ORNL), Oak Ridge, TN (United States). Atmospheric Radiation Measurement (ARM) Archive; Oak Ridge National Lab. (ORNL), Oak Ridge, TN (United States). Atmospheric Radiation Measurement (ARM) Data Center, https://doi.org/10.5439/1663226, 2021d.

Nath, D., Venkat Ratnam, M., Patra, A. K., Krishna Murthy, B. V., and Bhaskar Rao, S. V.: Turbulence characteristics over tropical station Gadanki (13.5°N, 79.2°E) estimated using high-resolution GPS radiosonde data, Journal of Geophysical Research: Atmospheres, 115, https://doi.org/10.1029/2009JD012347, 2010.

Pastore, D. M., Greenway, D. P., Stanek, M. J., Wessinger, S. E., Haack, T., Wang, Q., and Hackett, E. E.: Comparison of Atmospheric Refractivity Estimation Methods and Their Influence on Radar Propagation Predictions, Radio Science, 56, e2020RS007244, https://doi.org/10.1029/2020RS007244, 2021.

Qiu, S., Zheng, X., Painemal, D., Terai, C. R., and Zhou, X.: Daytime variation in the aerosol indirect effect for warm marine boundary layer clouds in the eastern North Atlantic, Atmospheric Chemistry and Physics, 24, 2913–2935, https://doi.org/10.5194/acp-24-2913-2024, 2024.

Ralph, F. M.: Using Radar-Measured Radial Vertical Velocities to Distinguish Precipitation Scattering from Clear-Air Scattering, Journal of Atmospheric and Oceanic Technology, 12, 257–267, https://doi.org/10.1175/1520-0426(1995)012<0257:URMRVV>2.0.CO;2, 1995.

https://doi.org/10.5194/egusphere-2025-4434
Preprint. Discussion started: 4 October 2025

Rémillard, J. and Tselioudis, G.: Cloud Regime Variability over the Azores and Its Application to Climate Model Evaluation, Journal of Climate, 28, 9707–9720, https://doi.org/10.1175/JCLI-D-15-0066.1, 2015.

Riddle, A. C., Hartten, L. M., Carter, D. A., Johnston, P. E., and Williams, C. R.: A Minimum Threshold for Wind Profiler Signal-to-Noise Ratios, Journal of Atmospheric and Oceanic Technology, 29, 889–895, https://doi.org/10.1175/JTECH-D-11-00173.1, 2012.

Rogers, R. R., Ecklund, W. L., Carter, D. A., Gage, K. S., and Ethier, S. A.: Research Applications of a Boundary-Layer Wind Profiler, Bulletin of the American Meteorological Society, 74, 567–580, https://doi.org/10.1175/1520-0477(1993)074<0567:RAOABL>2.0.CO;2, 1993.

Sullivan, R., Keeler, E., Billesbach, D., and Pal, S.: 30ecor (a1), Oak Ridge National Laboratory (ORNL), Oak Ridge, TN (United States). Atmospheric Radiation Measurement (ARM) Archive; Oak Ridge National Laboratory (ORNL), Oak Ridge, TN (United States). Atmospheric Radiation Measurement (ARM) Data Center, https://doi.org/10.5439/1879993, 1997.

Tokay, A., Petersen, W. A., Gatlin, P., and Wingo, M.: Comparison of Raindrop Size Distribution Measurements by Collocated Disdrometers, Journal of Atmospheric and Oceanic Technology, 30, 1672–1690, https://doi.org/10.1175/JTECH-D-12-00163.1, 2013.

Tridon, F., Battaglia, A., Kollias, P., Luke, E., and Williams, C. R.: Signal Postprocessing and Reflectivity Calibration of the Atmospheric Radiation Measurement Program 915-MHz Wind Profilers, Journal of Atmospheric and Oceanic Technology, 30, 1038–1054, https://doi.org/10.1175/JTECH-D-12-00146.1, 2013.

Vassilicos, J. C.: Dissipation in Turbulent Flows, Annual Review of Fluid Mechanics, 47, 95–114, https://doi.org/10.1146/annurev-fluid-010814-014637, 2015.

Wagner, M., Gerstoft, P., and Rogers, T.: Estimating refractivity from propagation loss in turbulent media, Radio Science, 51, 1876–1894, https://doi.org/10.1002/2016RS006061, 2016.

Wang, D. and Bartholomew, M. J.: Laser Disdrometer Instrument Handbook, DOE ARM Climate Research Facility, Pacific Northwest National Laboratory, Richland, Washington, https://doi.org/10.2172/1226796, 2023.

Wang, D., Giangrande, S. E., Feng, Z., Hardin, J. C., and Prein, A. F.: Updraft and Downdraft Core Size and Intensity as Revealed by Radar Wind Profilers: MCS Observations and Idealized Model Comparisons, Journal of Geophysical Research: Atmospheres, 125, e2019JD031774, https://doi.org/10.1029/2019JD031774, 2020.

Wang, J., Wood, R., Jensen, M. P., Christine Chiu, J., Liu, Y., Lamer, K., Desai, N., Giangrande, S. E., Knopf, D. A., Kollias, P., Laskin, A., Liu, X., Lu, C., Mechem, D., Mei, F., Starzec, M., Tomlinson, J., Wang, Y., Yum, S. S., Zheng, G., Aiken, A. C., Azevedo, E. B., Blanchard, Y., China, S., Dong, X., Gallo, F., Gao, S., Ghate, V. P., Glienke, S., Goldberger, L., Hardin, J. C., Kuang, C., Luke, E. P., Matthews, A. A., Miller, M. A., Moffet, R., Pekour, M., Schmid, B., Sedlacek, A. J., Shaw, R. A., Shilling, J. E., Sullivan, A., Suski, K., Veghte, D. P., Weber, R., Wyant, M., Yeom, J., Zawadowicz, M., and Zhang, Z.: Aerosol and Cloud Experiments in the Eastern North Atlantic (ACE-ENA), Bulletin of the American Meteorological Society, 103, E619–E641, https://doi.org/10.1175/BAMS-D-19-0220.1, 2022.

Wang, Q., Alappattu, D. P., Billingsley, S., Blomquist, B., Burkholder, R. J., Christman, A. J., Creegan, E. D., Paolo, T. de, Eleuterio, D. P., Fernando, H. J. S., Franklin, K. B., Grachev, A. A., Haack, T., Hanley, T. R., Hocut, C. M., Holt, T. R., Horgan, K., Jonsson, H. H., Hale, R. A., Kalogiros, J. A., Khelif, D., Leo, L. S., Lind, R. J., Lozovatsky, I., Planella-Morato, J., Mukherjee, S., Nuss, W. A., Pozderac, J., Rogers, L. T., Savelyev, I., Savidge, D. K., Shearman, R. K., Shen, L., Terrill, E., Ulate, A. M., Wang, Q., Wendt, R. T., Wiss, R., Woods, R. K., Xu, L., Yamaguchi, R. T., and Yardim, C.: CASPER: Coupled

https://doi.org/10.5194/egusphere-2025-4434
Preprint. Discussion started: 4 October 2025

Air–Sea Processes and Electromagnetic Ducting Research, Bulletin of the American Meteorological Society, 99, 1449–1471, https://doi.org/10.1175/BAMS-D-16-0046.1, 2018.

Wang, Y., Zheng, G., Jensen, M. P., Knopf, D. A., Laskin, A., Matthews, A. A., Mechem, D., Mei, F., Moffet, R., Sedlacek, A. J., Shilling, J. E., Springston, S., Sullivan, A., Tomlinson, J., Veghte, D., Weber, R., Wood, R., Zawadowicz, M. A., and Wang, J.: Vertical profiles of trace gas and aerosol properties over the eastern North Atlantic: variations with season and synoptic condition, Atmospheric Chemistry and Physics, 21, 11079–11098, https://doi.org/10.5194/acp-21-11079-2021, 2021.

White, A. B., Lataitis, R. J., and Lawrence, R. S.: Space and Time Filtering of Remotely Sensed Velocity Turbulence, Journal of Atmospheric and Oceanic Technology, 16, 1967–1972, https://doi.org/10.1175/1520-0426(1999)016<1967:SATFOR>2.0.CO;2, 1999.

Williams, C. R.: Reflectivity and Liquid Water Content Vertical Decomposition Diagrams to Diagnose Vertical Evolution of Raindrop Size Distributions, Journal of Atmospheric and Oceanic Technology, 33, 579–595, https://doi.org/10.1175/JTECH-D-15-0208.1, 2016.

Williams, C. R., Barrio, J., Johnston, P. E., Muradyan, P., and Giangrande, S. E.: Calibrating radar wind profiler reflectivity factor using surface disdrometer observations, Atmospheric Measurement Techniques, 16, 2381–2398, https://doi.org/10.5194/amt-16-2381-2023, 2023.

Wood, R.: Stratocumulus Clouds, Monthly Weather Review, 140, 2373–2423, https://doi.org/10.1175/MWR-D-11-00121.1, 2012.

Wood, R., Wyant, M., Bretherton, C. S., Rémillard, J., Kollias, P., Fletcher, J., Stemmler, J., Szoeke, S. de, Yuter, S., Miller, M., Mechem, D., Tselioudis, G., Chiu, J. C., Mann, J. A. L., O'Connor, E. J., Hogan, R. J., Dong, X., Miller, M., Ghate, V., Jefferson, A., Min, Q., Minnis, P., Palikonda, R., Albrecht, B., Luke, E., Hannay, C., and Lin, Y.: Clouds, Aerosols, and Precipitation in the Marine Boundary Layer: An Arm Mobile Facility Deployment, Bulletin of the American Meteorological Society, 96, 419–440, https://doi.org/10.1175/BAMS-D-13-00180.1, 2015.

Wyngaard, J. C. and LeMone, M. A.: Behavior of the Refractive Index Structure Parameter in the Entraining Convective Boundary Layer, Journal of the Atmospheric Sciences, 37, 1573–1585, https://doi.org/10.1175/1520-0469(1980)037<1573:BOTRIS>2.0.CO;2, 1980.